


Cite this: *RSC Adv.*, 2021, 11, 17871

Unsymmetrical pentamethine cyanines for visualizing physiological acidities from the whole-animal to the cellular scale with pH-responsive deep-red fluorescence†

Yicheng Wang,^{‡a} Zuhai Lei,^{‡a} Cong Wang,^a Chong Cao,^a Jiayi Hu,^a Ling Du,^{*b} Limei Han^{*a} and Cong Li^{ib*}

Acidity plays an important role in numerous physiological and pathological events. Non-invasively monitoring pH dynamics would be valuable for understanding pathological processes and optimizing therapeutic strategies. Although numerous near-infrared (NIR) fluorophores have been developed to monitor acidification *in vivo*, the experimental results are difficult to verify at the molecular or cellular level using a fluorescence microscope or flow cytometer due to the lack of lasers with excitation wavelengths in the NIR wavelength range. This work presents a sequential condensation strategy for obtaining unsymmetrical pentamethine cyanines with fine-tuned pK_a values and improved yields. These deep-red fluorophores with pH responsiveness can not only be used to monitor acidification in live cells using confocal microscopic imaging and flow cytometry, but they can also be used to non-invasively identify infected tissue with a low pH value in live mouse models. In addition, the acidity in infected tissue slices was verified under a conventional confocal microscope. Overall, this work demonstrates a new synthetic method with improved yields for unsymmetrical pentamethine cyanines that can report acidity. These pH-responsive deep-red fluorophores not only provide new tools for accessing pH-associated physiological and pathological events, but they can also help in understanding *in vivo* imaging results at the molecular or cellular level due to their detectability by multiple imaging instruments.

Received 20th March 2021
Accepted 1st May 2021

DOI: 10.1039/d1ra02217b

rsc.li/rsc-advances

Introduction

Acidity plays important roles in numerous physiological and pathological events. For example, acidification accompanies the maturity of intracellular organelles such as lysosomes and autophagosomes in normal cells.¹ Additionally, due to the reprogramming of glucose metabolism from oxidative phosphorylation to glycolysis in cancer cells, the acidification of the extracellular matrix is considered to be a hallmark of solid tumors regardless of their phenotypes or genotypes.² Acidity plays important roles in developing the tumor microenvironment. For instance, extracellular acidification suppresses immune responses by promoting the phenotypic transition of macrophages and deactivating the effective T cells.³

Furthermore, a temporal and spatial correlation was demonstrated between extracellular acidity and tissue malignancy in tumor invasive margins.^{4,5} Therefore, non-invasively monitoring pH dynamics in live cells, small animals and excised tissues would not only provide indispensable information for accessing the physiological and pathological processes, but also benefit therapeutic responses *via* intra-operative delineation of tumor invasive margins during surgery^{6,7} and guiding immune checkpoint therapy by evaluating the immune microenvironment in advance.⁸

Fluorescent probes have emerged as an essential tool in monitoring pH with high sensitivity, accuracy and safety.⁹ Fluorescence in the near-infrared region (NIR) (700–1700 nm) is preferable for *in vivo* imaging studies due to the deep tissue penetration and minimum background noise.^{10,11} Although NIR fluorescent probes show advantages for *in vivo* imaging studies, their fluorescence signals are difficult to detect in cell cultures and *ex vivo* tissue samples using conventional confocal fluorescence microscopy and flow cytometry due to the lack of lasers with wavelengths in the NIR range.¹² The above challenge makes it difficult to verify *in vivo* experimental results from NIR fluorescent probes at the cellular and molecular levels *via ex vivo* or *in vitro* imaging studies. Deep-red fluorophores with

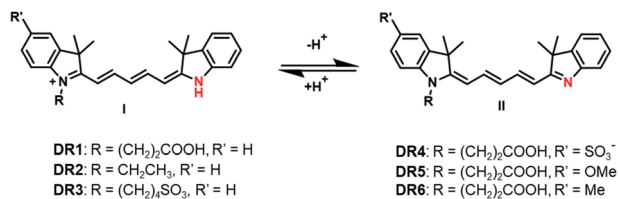
^aMinhang Hospital and Key Laboratory of Smart Drug Delivery, Ministry of Education, School of Pharmacy, Fudan University, Zhangheng Road 826, Shanghai, 201203, China. E-mail: congli@fudan.edu.cn

^bKey Laboratory of Digestive Cancer Full Cycle Monitoring and Precise Intervention of Shanghai Municipal Health Commission, Minhang Hospital, Fudan University, Xingsong Road 170, Shanghai, 201100, China

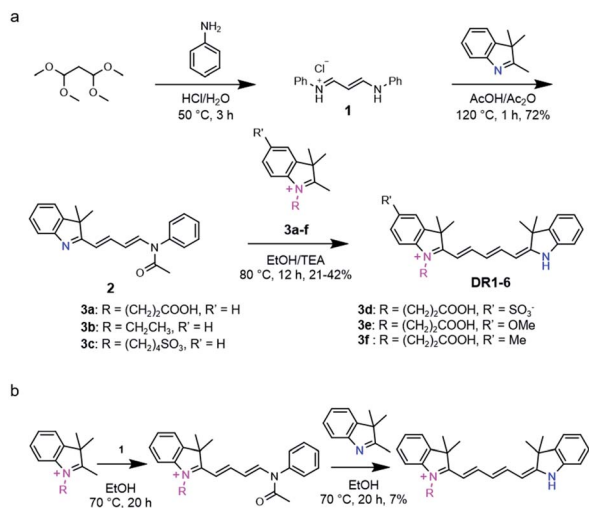
† Electronic supplementary information (ESI) available. See DOI:10.1039/d1ra02217b

‡ These authors contributed equally to this work.





Scheme 1 The chemical structures of the unsymmetrical pentamethine cyanines upon protonation and deprotonation.



Scheme 2 (a) The sequential condensation strategy providing the desired unsymmetrical pentamethine cyanine fluorophores. (b) The adverse condensation sequence that failed to provide the desired unsymmetrical cyanines with satisfactory yields.

absorption and emission wavelengths in the range of 620–680 nm have attracted attention because they show high tissue penetration depth and can be excited by He–Ne lasers (633 nm), which are widely equipped in confocal fluorescence microscopes and flow cytometers.¹³ However, only a few deep-red

fluorophores have been reported to sense physiologic acidity.^{14,15} As pH responsive deep-red fluorophores, unsymmetrical pentamethine cyanines can visualize physiologic acidity with high molar extinction coefficients, good photophysical stabilities and satisfactory quantum yields.^{16,17} However, current synthetic strategies for unsymmetrical pentamethine cyanines suffer from unsatisfactory overall yield^{16,18} and inconvenience in adjusting their pK_a values. Additionally, it is also difficult to covalently conjugate these cyanine fluorophores to targeting biomolecules or polymers. Therefore, strategies for the development of unsymmetrical pentamethine cyanines with improved yields, tuneable pK_a value and conjugation ability are urgently needed.

In this work, we report a sequential condensation strategy for unsymmetrical pentamethine cyanines with improved yields as high as 42%. Using this strategy, a series of unsymmetrical pentamethine cyanine derivatives, **DR1–6**, with pK_a values of 6.8–7.4 were synthesized (Scheme 1). Their photophysical properties as a function of pH were first investigated. The fluorophore **DR1** with a pK_a of 7.0 was then selected and successfully used to monitor pH fluctuations in the cytoplasm of live cells *via* both a fluorescence microscope and flow cytometer. **DR1** non-invasively visualized infection-induced tissue acidity in the mouse abdomen *via in vivo* fluorescence imaging. Furthermore, *ex vivo* fluorescence microscopic images verified the infection-induced acidification in the excised intestinal and peritoneum tissues. In addition, the carboxyl-group-modified in **DR1** provides convenience for labelling proteins, nanoparticles or other functional macromolecules.

Results and discussion

Synthesis of unsymmetrical pentamethine cyanines DR1–6

The general synthetic route of **DR1–6** is shown in Scheme 2a. The probes were developed *via* the condensation of malonaldehyde bis(phenylimine) with two different indole derivatives. To optimize the overall yield, different reaction conditions, such as the use of toluene/*n*-butyl alcohol, acetic

Table 1 Photophysical parameters of the unsymmetrical pentamethine cyanines^a

Comp.	λ _{Abs(max-OH)} /nm	λ _{Abs(max-H)} /nm	λ _{Em} /nm	Δλ _{ST} /nm	pK _a	Φ _{fl}
DR1	486	637	661	24	7.01	0.29 ^b 0.17 ^c
DR2	463	635	658	23	6.80	0.18 ^b 0.10 ^c
DR3	488	636	660	24	7.34	0.19 ^b 0.14 ^c
DR4	475	635	661	26	6.99	0.20 ^b 0.18 ^c
DR5	500	647	677	30	7.31	0.04 ^b 0.02 ^c
DR6	497	641	667	26	7.41	0.19 ^b 0.09 ^c

^a λ_{Abs(max-OH)} and λ_{Abs(max-H)} are the absorption maxima of the alkaline and acidic forms, respectively. λ_{Em} is the emission maximum. Δλ_{ST} is the Stokes shift. Φ_{fl} is the quantum yield. ^b Fluorescence quantum yields of compounds under acidic conditions (pH 4.0, PBS). ^c Fluorescence quantum yields of compounds in a physiological environment (pH 6.75, PBS).



anhydride/sodium acetate and ethanol/triethylamine, were tested. The results demonstrated that the ethanol/triethylamine combination is superior to the others.

Interestingly, we found that the reaction sequence was critical to the yields of the unsymmetrical cyanines. 2,3,3-Trimethyl-3H-indole first reacted with **1** to give intermediate **2**, which further reacted with N-substituted indoles **3a–f** to afford the final products **DR1–6**. In this way, the desired products were obtained with higher overall yields (42%) compared to that (yield: 7%) obtained using the adverse condensation sequence reported by Clear *et al.*¹⁹ (Scheme 2b). This experimental result can be attributed to the different reactivities of N-substituted and non-N-substituted indoles. The electron-withdrawing quaternary ammonium could enhance the reactivity of the 2-methyl on the indole salts in comparison to that of non-N-substituted indoles. Therefore, the indole salts (**3a–f**) could react with intermediates **2** more effectively than the non-N-substituted indoles (Scheme 2b).

Photophysical properties of DR1–6

The photophysical parameters of **DR1–6** are summarized in Table 1. The pH-dependent absorption and emission of the fluorophores were measured in phosphate buffers (PBS) with different pH values. In the UV-vis absorption spectra of **DR1–6**, two major absorption bands were observed (Fig. 1). As the pH was increased, the absorption at 630–650 nm diminished but the absorption at 460–500 nm increased, indicating a conversion between the protonated state (I) and deprotonated state (II) of these fluorophores (Scheme 1, Fig. S1†). The pH-dependent emission spectra and relative fluorescence intensity variation of **DR1–6** are shown in Fig. 2. Strong fluorescence intensity was found under acidic conditions for all fluorophores, and decreased gradually with increasing pH. The signal “ON” state of the non-N-alkylated unsymmetrical pentamethine cyanines

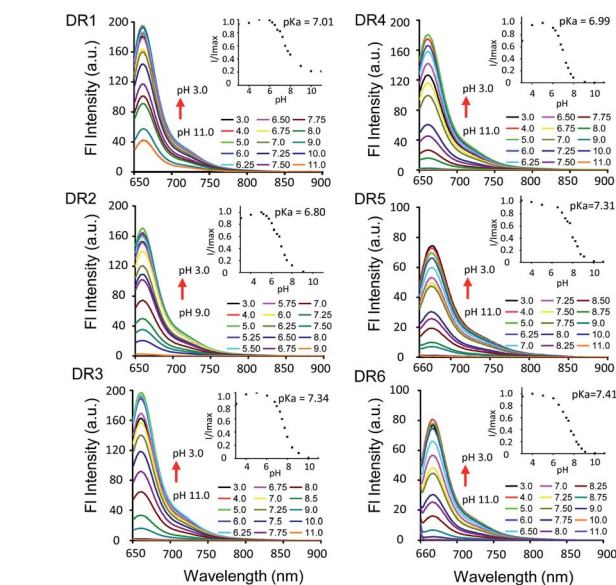


Fig. 2 Fluorescence spectra of **DR1–6** (1×10^{-6} M, DMSO/PBS = 1/1000) as a function of the pH value. The insets show the pH-dependent intensity variations.

in acid conditions can be explained by an electron push-pull resonance effect between the two indole rings.²⁰ The abstraction of the proton from the indole rings destroys this resonance and leads to a non-fluorescent form.²¹ This pH response mechanism was verified by ¹H NMR (Fig. S1†) using **DR6** as an example.

We performed density functional theory (DFT) calculations at the B3LYP/6-31 G(d,p) level to study the mechanism of the photophysical changes upon acidification (Fig. 3). In the protonated form, the π electrons of the HOMO are located over the whole π -conjugated chain, but the LUMO is mainly positioned at the center of the conjugated polymethine, where the bond length alternation (BLA) is minimal. This electron delocalization pattern in the HOMO/LUMO is a classic feature of cyanine dyes. In the deprotonated form, the π electrons on the HOMO and LUMO are mainly located on the π -conjugated

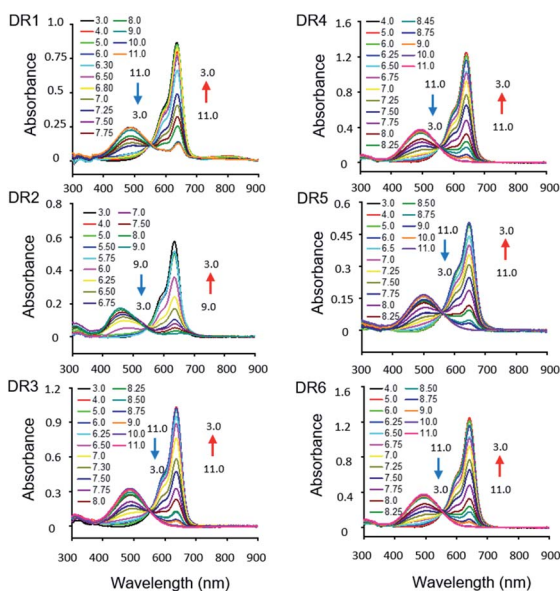


Fig. 1 Absorption spectra of **DR1–6** (2×10^{-5} M, DMSO/PBS = 1/50) as a function of pH.

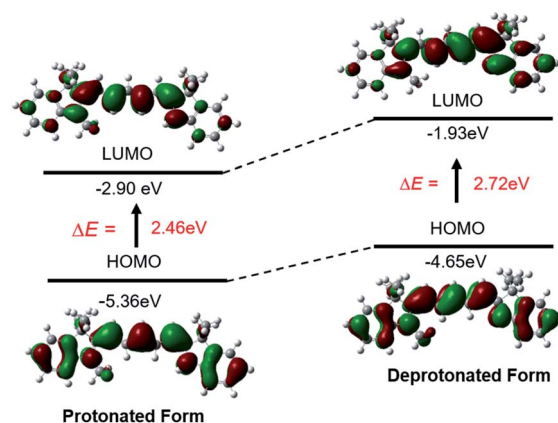


Fig. 3 Theoretical calculations of the photophysical properties of the unsymmetrical pentamethine cyanine dye in its protonated and deprotonated forms.



polymethine and conjugated polymethine-indole, respectively. In other words, the deprotonated molecule loses its “cyanine limit” structure, which is characterized by a sharp and intense absorption in the NIR region. Additionally, the energy gap between the HOMO and LUMO is much smaller for the protonated structure, consistent with its long-wavelength absorption and emission spectra.²²

For **DR1–3**, the R' group at the 5' position of the indole was fixed as hydrogen, and the R group was an N-substituted alkyl chain with a terminal group such as carboxylic acid or sulfonic acid. Their absorption and emission spectra were not affected by the substituent at the terminal of the N-alkyl chain. A bathochromic shift of about 16 nm was observed with electron-donating substitution on the indole moiety by comparison in the spectra of **DR4–6**, in which the R group was fixed as N-substituted alkyl chain with a terminal carboxyl group and the R' groups were groups with different electron-donating capabilities. Time-dependent density functional theory (TDDFT) calculations at the B3LYP/6-311 G(d,p) level were performed to study the photophysical properties of all the fluorophores. Schematic drawings of the HOMO and LUMO orbitals, the excitation energies and the corresponding absorption wavelength of **DR1–6** are shown in Fig. S1† and Table S1†. The TDDFT studies indicated that the HOMO–LUMO energy gaps of **DR5** and **DR6** were higher than that of **DR1**, which is in good agreement with the observation that the absorption wavelengths of **DR5** and **DR6** are larger than that of **DR1**. The oscillator strength of **DR5** was lower than those of other fluorophores, which may explain the significant reduction of its quantum yield. The calculated absorption maxima of the deprotonated dyes were consistent with the experimental data. However, the calculated absorption maxima of the protonated dyes were shorter than those obtained experimentally. TDDFT calculations may underestimate excitation or emission wavelengths due to the limitations of the exchange-correlation functional.^{23,24}

The pK_a values of **DR1–6** are shown in Fig. 2. The pK_a value of **DR1** was determined to be 7.01. **DR2** and **DR3** with ethyl and butyl sulfonic acid substitution showed pK_a values of 6.80 and 7.34, respectively. It appears that these functional groups affect the space charge distribution and hence the pK_a of the fluorophores.²⁰ The sulfo group served as a water-soluble group and did not affect the pK_a value (**DR4**). **DR5** and **DR6** with electron-donating group substitution showed increased pK_a values of 7.31 and 7.41, respectively. These results indicated that the pK_a values of the unsymmetrical pentamethine cyanines can be fine-tuned by ingeniously introducing functional groups on an indole moiety.

DR1 for imaging intracellular acidity in live cancer cells

Since **DR1** had the highest quantum yield and an appropriate pK_a , we then employed **DR1** as a fluorescent pH probe for cell culture studies under confocal laser scanning microscopy. The cytotoxicity of **DR1** towards HeLa cells was first determined using a Cell Counting Kit-8 (CCK-8) assay (Fig. S4†). The relative viabilities of the HeLa cells were above 90% with probe

concentrations of up to 50 μM , indicating the low cytotoxicity and good biocompatibility of **DR1**. The selectivity of **DR1** was examined in the presence of various other coexisting species to determine the potential interference under physiological conditions. As shown in Fig. S5,† the fluorescence intensity in pH 4.0 PBS increased approximately 3-fold in comparison to that in pH 7.0 PBS. However, no significant variations in the fluorescence signal intensity were observed in the presence of potential interferents (NH_4^+ , Co^{2+} , Ca^{2+} , Mg^{2+} , Fe^{2+} , Fe^{3+} , H_2O_2 , glucose, glutathione and cysteine), except for Cu^{2+} . Cu^{2+} may oxidize the unsaturated bonds and hence attenuate the fluorescence intensity. Considering the intracellular concentration of free Cu^{2+} (10^{-18} M),²³ which is far below the tested concentration (200 μM), its potential disruption to the pH-responsive fluorescence should be minimal. The performance of **DR1** for monitoring the intracellular acidity in live cells was investigated. HeLa cells were incubated with **DR1** (10 μM) for 12 h. The medium was then replaced with high- K^+ buffers with different pH values.²⁴ As shown in Fig. 4a, the fluorescence intensity decreased proportionally as the pH value was increased from 5.0 to 8.0. The mean intensities at different pH values in the cells were further quantified using flow cytometry (Fig. 4b, c). **DR1** exhibited pH-responsive fluorescence behavior in live cells with a good linear relationship in the range of pH 5.0–8.0. The above results confirm that **DR1** can be used to monitor pH changes in cell cultures under a fluorescence microscope.

DR1 for visualizing infection-induced acidity in mouse models and excised tissue sections

Encouraged by the *in vitro* imaging studies, we further evaluated the use of **DR1** for visualizing pH changes in infection-

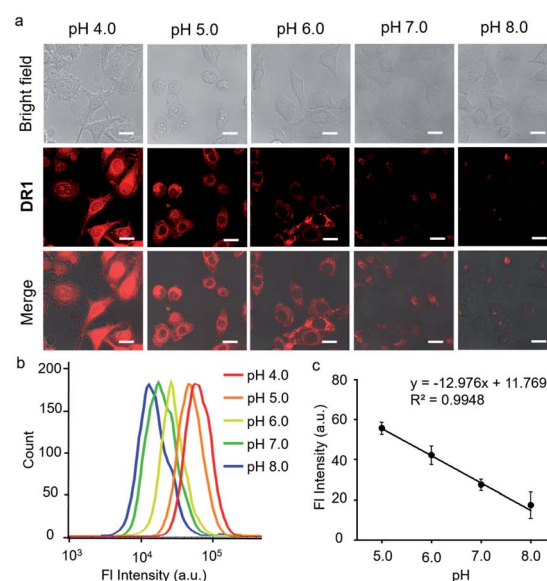


Fig. 4 (a) Bright field, fluorescence, and merged images of HeLa cells treated with **DR1** at pH 4.0, 5.0, 6.0, 7.0, and 8.0 (Ex: 633 nm), scale bar = 20 μm . (b) Flow cytometry of HeLa cells treated with **DR1** at pH 4.0, 5.0, 6.0, 7.0, and 8.0. (c) The linear relationship between the fluorescence intensity and pH from the data in Fig. 3b. Error bars represent the mean standard deviation (S.D.), $n = 3$.



associated animal models that were developed by intraperitoneally injecting lipopolysaccharide (LPS, 10 mg kg⁻¹). Acute inflammatory symptoms such as tissue acidification have been reported after LPS administration.^{15,25} The mouse infection models were randomly divided into two groups. One group was used as a negative control without the administration of **DR1**. The other group was injected intraperitoneally with **DR1** at 5 h post administration of LPS. Additionally, a group of normal mice were treated with **DR1** as the positive control. As shown in Fig. 5a, the abdomens of the mouse models treated with LPS alone showed almost no fluorescence. In contrast, the mice treated with LPS followed by **DR1** exhibited significantly higher fluorescence intensity than those of the healthy mice treated with **DR1**. Quantitative studies revealed that the fluorescence intensity in the abdomen increased approximately 7-fold in comparison with that of the normal mice (Fig. 5b, S6†). Importantly, acidity-triggered fluorescence enhancement in the infected tissues excised from the models was successfully observed under laser confocal microscopy. As shown in Fig. 5c and d, both the intestinal and peritoneum tissues of the LPS-treated animals exhibited significantly higher fluorescence intensity than those treated with PBS alone, which is consistent with the *in vivo* results. Notably, both the *in vivo* and *ex vivo* results based on **DR1** fluorescence imaging were in good agreement with the pH values (6.60–6.90) of the intraabdominal

tissue fluids measured using a pH meter (Fig. 5e). Collectively, these results clearly demonstrated that **DR1** can verify the tissue acidification observed in an *in vivo* animal study at the excised tissue and cell scales.

Conclusions

In summary, we developed a series of deep-red emissive and pH-sensitive fluorophores, **DR1–6**, using a sequence-dependent synthesis strategy. The pK_a values of these fluorophores can be finely modulated *via* introducing selected substituents on the indole moiety. Compared with NIR fluorescent probes, these deep-red fluorophores not only provide new tools for imaging pH-associated physiological and pathological events, but they also help in the understanding of events observed under *in vivo* conditions at the molecular or cellular level due to their visibility using a conventional fluorescence microscope and flow cytometer.

Experimental section

General information

All chemical reagents and solvents for probe synthesis were obtained from Adamas Reagent Co. Ltd. unless otherwise specified. 1-(2-Carboxyethyl)-5-methoxy-2,3,3-trimethyl-3H-indole and 1-(2-carboxyethyl)-5-methyl-2,3,3-trimethyl-3H-indole were purchased from Merck Co. Ltd. Culture media, fetal bovine serum (FBS), trypsin, penicillin and streptomycin were purchased from Thermo-Fisher Scientific Inc. Cell Counting Kit-8 (CCK-8) was supplied by Yeasen (China). ¹H and ¹³C NMR spectra were recorded using a 400 MHz (Varian, USA) or 600 MHz (Bruker, USA) NMR spectrometer. High resolution electron spray ionization (HR-ESI) mass spectra were obtained using a Q-TOF 2 (Micromass, USA) or AB 5600+ Q-TOF mass spectrometer (AB Sciex, USA). All pH measurements were performed using a Mettler Toledo (Switzerland) MP220 pH meter. An Inlab Micro Pro-ISM electrode was employed to measure the pH values *in vivo*. Absorption spectra were obtained using a SHIMADZU (Japan) UV-2550 spectrophotometer. Fluorescence spectra were collected using a SHIMADZU (Japan) RF-5301 PC fluorophotometer. Fluorescence microscopy images were obtained using a Leica (Germany) DMI4000D inverted microscope and a Zeiss (Germany) LSM 710 confocal microscope. Flow cytometric studies were analyzed using a BD (USA) FACSaria II flow cytometer. Small animal imaging was acquired in an IVIS Spectrum *In Vivo* Imaging System (Caliper Life Sciences, USA).

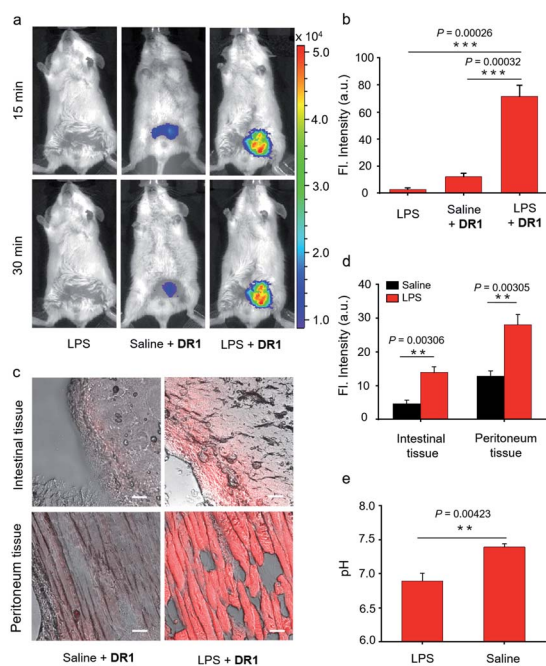


Fig. 5 (a) Representative fluorescence images of animals treated with LPS alone, saline followed by **DR1**, and LPS followed by **DR1** (Ex: 640 nm, Em: 680–700 nm). (b) Mean fluorescence intensity in the abdominal region 15 min after the administration of **DR1** ($n = 3$). (c) Fluorescence microscopy images of fresh intestinal and peritoneum tissue slices of mice treated with **DR1** alone or LPS followed by **DR1** (Ex = 633 nm). Scale bar = 50 μ m. (d) Mean fluorescence intensity of the tissue slices ($n = 3$). (e) Intraabdominal fluid pH values (measured with a pH meter) 30 min after treatment with LPS or saline ($n = 3$). Error bars represent the mean deviation (S.D.), P values were calculated using two-tailed Student's t -tests.

Photospectroscopic studies

Stock solutions of **DR1–6** were prepared in dimethyl sulfoxide (DMSO) with a concentration of 1×10^{-3} M.

Absorption spectra. Working solutions (2×10^{-5} M) were prepared by diluting the stock solution in PBS solutions with pH values ranging from 3.0 to 11.0. All absorption spectra were recorded in a quartz cuvette (10 \times 5 mm) at room temperature (r.t.). The scanning wavelength range was 300–900 nm and scanning speed was 1.0 nm s⁻¹ (slit width: 5 nm).



Emission spectra. Working solutions (1×10^{-6} M) were prepared by diluting the stock solution in PBS solutions with pH values ranging from 3.0 to 11.0. All emission spectra were obtained using a photomultiplier tube at r.t. All compounds were excited at their maximum absorption wavelength.

Calculations of pK_a values. The normalized fluorescence intensities were plotted against the pH values, and the sigmoidal plots were fitted to sigmoidal curves (eqn (1)) using OriginPro 9.0. A_1 and A_2 represent the maximum and minimum of fluorescence intensity, respectively. The pK_a values were determined as x_0 from the equation below.

$$y = A_2 + \frac{A_1 - A_2}{1 + e^{(x-x_0)/d_x}} \quad (1)$$

x : pH; y : fluorescence intensity at x ; d_x : time constant; A_1 : initial value of fluorescence intensity; A_2 : final value of fluorescence intensity.

Calculations of pK_a values

The fluorescence quantum yields were determined using Rhodamine B²⁶ as a standard and calculated according to eqn (2):

$$\Phi_{\text{fl}} = \Phi_{\text{R}} \times \frac{I}{I_{\text{R}}} \times \frac{A_{\text{R}}}{A} \times \frac{n^2}{n_{\text{R}}^2} \quad (2)$$

where Φ_{fl} represents the quantum yield; I is the integrated area under the emission spectrum; A is the absorbance; n is the refractive index of the solution; and the subscript R refers to the reference fluorophore Rhodamine B. The UV-vis absorbance at the excitation wavelength of the sample and standard was measured in diluted solutions at $A < 0.05$ to avoid inner filter effects. The integrated fluorescence intensities of the samples and reference were recorded at the same excitation wavelength.

Synthesis of DR1–6

General statement. First, malonaldehyde bis(phenylimine) **1** was prepared by reaction between 1,1,3,3-tetramethoxypropane and aniline under acidic conditions.²⁷ Then, 2,3,3-trimethyl-3H-indole was condensed with **1** to yield intermediate **2** in the presence of acetic acid and acetic anhydride.²⁸ The intermediates **3a–f** were obtained *via* alkylation of the indole with the corresponding halogenated alkanes.^{29,30} Then, the indole derivatives **3a–f** were condensed with the intermediate **2** to obtain **DR1–6**, respectively.

Synthesis of malonaldehyde bis(phenylimine) (1**).** A solution of hydrochloric acid (75 mL, 0.8 mol L⁻¹) and aniline (3.7 mL, 40 mmol) was added dropwise to a solution of hydrochloric acid (90 mL, 0.6 mol L⁻¹) and 1,1,3,3-tetramethoxypropane (5.3 mL, 30 mmol), followed by stirring at 50 °C for 3 h. The precipitate was isolated by filtration to give 7.5 g (90% yield) of **1** as an orange solid.

Synthesis of intermediate **2.** 2,3,3-Trimethyl-3H-indole (2 g, 12.5 mmol) and **1** (3.84 g, 14.8 mmol) were dissolved in 20 mL of a mixed solvent (acetic acid : acetic anhydride = 1 : 1, v/v), and the solution was refluxed with stirring under argon for 1 hour at 120 °C. The mixture was cooled and diluted with ethyl acetate.

The resulting solution was extracted with saturated Na₂CO₃ aqueous solution, and the organic phase was dried over Na₂SO₄, filtered and evaporated. The residue was purified by column chromatography on silica gel with CH₂Cl₂ to obtain product **2** as a yellow solid (3 g, 72% yield).

Synthesis of 1-(2-carboxyethyl)-2,3,3-trimethyl-3H-indol-1-ium (3a**).** A mixture of 2,3,3-trimethyl-3H-indole (5 g, 31.4 mmol) and 3-iodopropionic acid (6.6 g, 33 mmol) was dissolved in toluene (20 mL), and the solution was stirred under argon at 100 °C for 3 h. The solvent was evaporated under vacuum. The residue was dissolved in water and washed with CH₃Cl to obtain **3a** as a yellow solid without further purification (5.8 g).

Synthesis of 1-ethyl-2,3,3-trimethyl-3H-indol-1-ium (3b**).** 2,3,3-Trimethyl-3H-indole (1 g, 6.29 mmol), iodoethane (5 g, 32.1 mmol) and toluene (20 mL) were mixed and refluxed under argon for 12 h. After cooling to room temperature, the mixture was filtered and the residue was washed with hexane and diethyl ether to obtain **3b** as a red solid without further purification (0.91 g).

Synthesis of 4-(2,3,3-trimethyl-3H-indol-1-ium-1-yl) butane-1-sulfonate (3c**).** 2,3,3-Trimethyl-3H-indole (3 g, 18.9 mmol), 1,4-butane sultone (5 g, 36.7 mmol) and 1,2-dichlorobenzene (20 mL) were mixed and heated at 110 °C with stirring for 12 h under argon. At the end of the reaction, the solution was cooled to room temperature and dropped into methyl ether in an ice bath. After precipitation, the red product was filtered, re-dissolved in 20 mL saturated sodium chloride solution, and extracted with chloroform. The organic layer was collected and evaporated, and the product was dried under vacuum without further purification (3.7 g).

Synthesis of 4-(2,3,3-trimethyl-3H-indol-1-ium-1-yl) butane-1-sulfonate (3d**).** 2,3,3-Trimethyl-3H-indole-5-sulfonate⁵ (2 g, 7.2 mmol) and 3-iodopropionic acid (1.73 g, 8.64 mmol) were dissolved in 1,2-dichlorobenzene (20 mL). The solution was stirred at 110 °C for 19 h. The supernatant was removed, and the residue was washed with 2-propanol and diethyl ether to obtain **3e** without further purification (0.91 g).

Synthesis of 1-(2-carboxyethyl)-5-methoxy-2,3,3-trimethyl-3H-indol-1-ium (3e**).** A mixture of 1-(2-carboxyethyl)-5-methoxy-2,3,3-trimethyl-3H-indole (1 g, 5.3 mmol) and 3-iodopropionic acid (1.16 g, 5.8 mmol) was dissolved in toluene (20 mL), and the solution was stirred under argon at 100 °C for 12 h. The supernatant was removed, and the residue was dissolved in water and washed with ethyl acetate. The aqueous layer was collected and evaporated, and the product was dried under vacuum to obtain **3e** without further purification (1.7 g).

Synthesis of 1-(2-carboxyethyl)-5-methyl-2,3,3-trimethyl-3H-indol-1-ium (3f**).** A mixture of 1-(2-carboxyethyl)-5-methyl-2,3,3-trimethyl-3H-indole (1 g, 5.7 mmol) and 3-iodopropionic acid (1.38 g, 6.9 mmol) was dissolved in 1,2-dichlorobenzene (20 mL), and the solution was stirred under argon at 120 °C for 12 h. The supernatant was removed, and the residue was dissolved in water and washed with CHCl₃. The aqueous phase was collected and evaporated, and the product was dried under vacuum to obtain **3f** without further purification (1.1 g).

Synthesis and characterization of DR1. A mixture of intermediate **2** (0.2 g, 0.6 mmol), the indole ammonium salt **3a**



(0.25 g, 0.72 mmol) and TEA (0.25 mL) in ethyl alcohol was refluxed for 12 h. The solution was cooled to room temperature and the solvent was removed under reduced pressure. The resulting product was purified by column chromatography using silica gel and CH₂Cl₂/MeOH (95/5) as the eluent to obtain **DR1** as a dark blue powder (0.128 g, 42% yield). ¹H NMR (600 MHz, methanol-*d*₄) δ 7.84 (t, *J* = 13.2 Hz, 1H), 7.67 (t, *J* = 13.1 Hz, 1H), 7.39 (d, *J* = 7.4 Hz, 1H), 7.37–7.29 (m, 3H), 7.26 (t, *J* = 7.7 Hz, 1H), 7.19 (t, *J* = 7.3 Hz, 1H), 7.07 (d, *J* = 7.8 Hz, 1H), 7.03 (t, *J* = 7.4 Hz, 1H), 6.41 (t, *J* = 12.4 Hz, 1H), 6.21 (d, *J* = 14.6 Hz, 1H), 5.95 (d, *J* = 12.8 Hz, 1H), 4.19–4.12 (m, 2H), 2.59 (t, *J* = 7.7 Hz, 2H), 1.64 (s, 6H), 1.47 (s, 6H). ¹³C NMR (151 MHz, methanol-*d*₄) δ 182.8, 179.6, 149.3, 148.4, 144.8, 144.5, 141.2, 129.3, 129.1, 125.9, 125.3, 123.5, 123.0, 116.7, 109.7, 100.6, 52.2, 41.4, 35.3, 28.4, 25.5. HRMS (Q-TOF) *m/z* [M + H]⁺ calcd for C₂₈H₃₁N₂O₂ 427.2380; found 427.2377.

Synthesis and characterization of DR2. A mixture of intermediate **2** (0.2 g, 0.6 mmol), the indole ammonium salt **3b** (0.22 g, 0.72 mmol) and TEA (0.25 mL) in ethyl alcohol was refluxed for 12 h. The solution was cooled to room temperature and the solvent was removed under reduced pressure. The resulting product was purified by column chromatography using silica gel and petroleum ether/ethyl acetate (95/5) as the eluent to obtain **DR2** as a dark blue powder (0.069 g, 30% yield). ¹H NMR (600 MHz, methanol-*d*₄) δ 7.89 (t, *J* = 13.2 Hz, 1H), 7.74 (t, *J* = 13.0 Hz, 1H), 7.40 (d, *J* = 7.4 Hz, 1H), 7.37 (d, *J* = 6.7 Hz, 2H), 7.32 (d, *J* = 7.8 Hz, 2H), 7.22–7.18 (m, 1H), 7.11–7.04 (m, 2H), 6.45 (t, *J* = 12.6 Hz, 1H), 6.19 (d, *J* = 14.4 Hz, 1H), 5.97 (d, *J* = 13.0 Hz, 1H), 3.98 (q, *J* = 7.2 Hz, 2H), 1.66 (s, 6H), 1.49 (s, 6H), 1.32 (t, *J* = 7.3 Hz, 3H). ¹³C NMR (151 MHz, methanol-*d*₄) δ 179.9, 165.5, 147.4, 145.8, 142.1, 139.6, 128.8, 127.4, 127.2, 123.8, 123.1, 121.9, 121.1, 114.1, 107.8, 107.3, 98.8, 49.9, 36.9, 28.7, 26.3, 23.7, 10.1. HRMS (Q-TOF) *m/z* [M + H]⁺ calcd for C₂₈H₃₃N 383.2608; found 383.2610.

Synthesis and characterization of DR3. A mixture of intermediate **2** (0.2 g, 0.6 mmol), the indole ammonium salt **3c** (0.21 g, 0.72 mmol) and TEA (0.25 mL) in ethyl alcohol was refluxed for 12 h. The solution was cooled to room temperature and the solvent was removed under reduced pressure. The resulting product was purified by column chromatography using silica gel and CH₂Cl₂/MeOH (95/5) as the eluent to obtain **DR3** as a dark blue powder (0.073 g, 25% yield). ¹H NMR (600 MHz, methanol-*d*₄) δ 7.82 (t, *J* = 13.2 Hz, 1H), 7.67 (t, *J* = 13.1 Hz, 1H), 7.38 (d, *J* = 7.3 Hz, 1H), 7.34–7.23 (m, 4H), 7.17 (td, *J* = 7.2, 1.5 Hz, 1H), 7.04 (t, *J* = 7.7 Hz, 2H), 6.42 (t, *J* = 12.5 Hz, 1H), 6.18 (d, *J* = 14.5 Hz, 1H), 5.94 (d, *J* = 12.9 Hz, 1H), 3.92 (t, *J* = 6.9 Hz, 2H), 2.89 (t, *J* = 6.9 Hz, 2H), 1.93–1.89 (m, 4H), 1.64 (s, 6H), 1.47 (s, 6H). ¹³C NMR (151 MHz, methanol-*d*₄) δ 180.4, 165.2, 146.9, 144.9, 142.7, 139.3, 127.2, 123.8, 123.2, 121.7, 121.0, 114.4, 107.9, 98.9, 50.0, 41.9, 26.4, 25.0, 23.6, 21.6. HRMS (Q-TOF) *m/z* [M + H]⁺ calcd for C₂₉H₃₄N₂O₃S 489.2217; found 489.2215.

Synthesis and characterization of DR4. A mixture of intermediate **2** (0.2 g, 0.6 mmol), the indole ammonium salt **3d** (0.22 g, 0.72 mmol) and TEA (0.25 mL) in ethyl alcohol was refluxed for 12 h. The solution was cooled to room temperature and the solvent was removed under reduced pressure. The

resulting product was purified by column chromatography using silica gel and CH₂Cl₂/MeOH (80/20) as the eluent to obtain **DR4** as a dark blue powder (0.063 g, 21% yield). ¹H NMR (600 MHz, methanol-*d*₄) δ 7.70 (dd, *J* = 8.2, 1.7 Hz, 1H), 7.68–7.62 (m, 2H), 7.42 (d, *J* = 7.9 Hz, 2H), 7.38 (d, *J* = 7.4 Hz, 1H), 7.31 (td, *J* = 7.6, 1.3 Hz, 1H), 7.20 (t, *J* = 7.4 Hz, 1H), 6.95 (d, *J* = 8.3 Hz, 1H), 6.35 (dt, *J* = 13.9, 5.1 Hz, 2H), 5.77 (d, *J* = 12.2 Hz, 1H), 4.05 (d, *J* = 9.3 Hz, 2H), 2.55 (t, *J* = 7.8 Hz, 2H), 1.63 (s, 6H), 1.45 (s, 6H). ¹³C NMR (151 MHz, methanol-*d*₄) δ 185.5, 180.0, 152.9, 146.8, 144.6, 138.5, 128.9, 127.6, 126.6, 126.3, 122.6, 120.8, 119.2, 116.6, 107.6, 99.8, 57.5, 53.2, 47.3, 35.1, 28.5, 24.7. HRMS (Q-TOF) *m/z* [M][−] calcd for C₂₈H₃₀N₂O₅S 505.1803; found 505.1799.

Synthesis and characterization of DR5. A mixture of intermediate **2** (0.2 g, 0.6 mmol), the indole ammonium salt **3e** (0.28 g, 0.72 mmol) and TEA (0.25 mL) in ethyl alcohol was refluxed for 12 h. The solution was cooled to room temperature and the solvent was removed under reduced pressure. The resulting product was purified by column chromatography using silica gel and CH₂Cl₂/MeOH (90/10) as the eluent to obtain **DR5** as a dark blue powder (0.093 g, 34% yield). ¹H NMR (400 MHz, methanol-*d*₄) δ 7.84–7.65 (m, 2H), 7.34 (dd, *J* = 7.6, 3.8 Hz, 1H), 7.26–7.18 (m, 2H), 7.14–7.06 (m, 2H), 6.98 (d, *J* = 3.1 Hz, 1H), 6.84 (dd, *J* = 8.3, 3.4 Hz, 1H), 6.38 (s, 1H), 6.03 (d, *J* = 13.7 Hz, 2H), 4.16 (t, *J* = 7.4 Hz, 2H), 3.78 (d, *J* = 3.7 Hz, 3H), 2.54 (d, *J* = 8.8 Hz, 2H), 1.62 (d, *J* = 4.0 Hz, 6H), 1.44 (d, *J* = 3.9 Hz, 6H). ¹³C NMR (151 MHz, methanol-*d*₄) δ 178.0, 176.8, 156.7, 141.4, 135.6, 127.2, 123.2, 121.1, 113.1, 112.3, 109.4, 108.1, 54.4, 49.4, 40.2, 33.8, 26.2, 24.1. HRMS (Q-TOF) *m/z* [M + H]⁺ calcd for C₂₉H₃₃N₂O₃ 457.2486; found 457.2483.

Synthesis and characterization of DR6. A mixture of intermediate **2** (0.2 g, 0.6 mmol), the indole ammonium salt **3f** (0.28 g, 0.72 mmol) and TEA (0.25 mL) in ethyl alcohol was refluxed for 12 h. The solution was cooled to room temperature and the solvent was removed under reduced pressure. The resulting product was purified by column chromatography using silica gel and CH₂Cl₂/MeOH (90/10) as the eluent to obtain **DR6** as a dark blue powder (0.081 g, 31% yield). ¹H NMR (600 MHz, methanol-*d*₄) δ 7.79 (t, *J* = 13.1 Hz, 1H), 7.65 (t, *J* = 12.9 Hz, 1H), 7.37 (d, *J* = 7.4 Hz, 1H), 7.34–7.26 (m, 2H), 7.18–7.12 (m, 2H), 7.07 (d, *J* = 7.9 Hz, 1H), 6.97 (d, *J* = 8.1 Hz, 1H), 6.38 (t, *J* = 12.5 Hz, 1H), 6.14 (d, *J* = 14.5 Hz, 1H), 5.94 (d, *J* = 12.9 Hz, 1H), 4.15–4.10 (m, 2H), 2.56 (t, *J* = 7.8 Hz, 2H), 2.33 (s, 3H), 1.61 (s, 6H), 1.45 (s, 6H). ¹³C NMR (151 MHz, methanol-*d*₄) δ 182.2, 179.2, 166.9, 148.3, 144.6, 142.2, 141.5, 133.6, 129.6, 129.1, 125.6, 124.9, 123.7, 123.0, 116.5, 109.7, 100.6, 52.0, 47.8, 41.7, 35.6, 28.4, 28.4, 25.6, 21.2. HRMS (Q-TOF) *m/z* [M + H]⁺ calcd for C₂₉H₃₃N₂O₂ 441.2537; found 441.2533.

In vitro studies

Cell culture. HeLa cells were purchased from the American Type Culture Collection (ATCC) and cultured in Dulbecco's modified Eagle's medium supplemented with 10% fetal bovine serum (FBS), 2 mmol L-glutamine, 1% penicillin, and streptomycin at 37 °C in a humidified atmosphere with 5% CO₂/95% air.

Cytotoxicity. The cell viability was determined using the CCK-8 assay. HeLa cells were plated in the 96-well plates with 5×10^3 cells per well and cultured for 12 h. Subsequently, the cells were exposed to DMEM media containing the indicated concentration of **DR1**. After 12 h of incubation, the cells were washed with PBS three times, and then 100 μ L fresh medium per well containing 10 μ L CCK-8 reagent was added. After incubation for another 4 h at 37 °C, the absorbance at 450 nm in each well was recorded. The viability of cells without any treatment was used as a control.

In vitro fluorescence imaging. HeLa cells were pretreated with DMEM containing **DR1** (10 μ M) for 12 h. The media was then replaced with high K^+ buffer (30 mM NaCl, 120 mM KCl, 1.0 mM $CaCl_2$, 0.50 mM $MgSO_4$, 1.0 mM NaH_2PO_4 , 5.0 mM glucose, 20 mM sodium acetate, 20 mM HEPES, 10 μ M nigericin, and 20 mM MES) of various pH values. After 15 min of incubation, cell imaging was carried out using the confocal fluorescence microscope (Ex = 633 nm).

Flow cytometry. HeLa cells were pretreated with DMEM containing **DR1** (10 μ M) for 12 h. The media were then replaced with high K^+ buffer of various pH values. After 15 min of incubation, the cells were detached using trypsin, collected by centrifugation and analyzed using flow cytometry.

In vivo studies

In vivo fluorescence imaging. All animal studies were performed in compliance with the guidelines set by the Chinese Committee of Management of Laboratory Animals and the overall project protocols were approved by the Ethics Committee of Fudan University. Male Balb/c mice (18–20 g) were purchased from Shanghai Slac Lab Animal Ltd (Shanghai, China). The mice were divided into three groups. Group one was injected intraperitoneally with LPS (200 μ L in PBS, 1.0 mg mL^{-1}). Group two was injected intraperitoneally with saline (200 μ L). After 5 h, the mice were injected intraperitoneally with **DR1** (200 μ L, 50 μ M). Group three was injected intraperitoneally with LPS (200 μ L in PBS, 1.0 mg mL^{-1}). After 5 h, the mice were injected intraperitoneally with **DR1** (200 μ L, 50 μ M). *In vivo* images were then taken at the indicated time (Ex = 640 nm, Em = 680–700 nm).

Fluorescence microscopy imaging. Male Balb/c mice of group one and group two were sacrificed 20 min after **DR1** injection. Their intestinal and peritoneum tissues were quickly dissected, frozen at -20 °C and sectioned consecutively with a thickness of 30 μ m. All slices were examined under a confocal microscope without fixation (Ex = 633 nm).

Conflicts of interest

There are no conflicts to declare.

Acknowledgements

This work was supported by the National Natural Science Foundation of China (No. 81771895, 21908030), the National Science Fund for Distinguished Young Scholars (822025019),

and the Program of Shanghai Science and Technology Committee (No. 19431900400, 18441900600 and 20S31903700).

Notes and references

- 1 J. R. Casey, S. Grinstein and J. Orłowski, *Nat. Rev. Mol. Cell Biol.*, 2010, **11**, 50–61.
- 2 R. J. Gillies, Z. Liu and Z. Bhujwalla, *Am. J. Physiol.*, 1994, **267**, C195–C203.
- 3 H. Sekine, M. Yamamoto and H. Motohashi, *Nat. Immunol.*, 2018, **19**, 1281–1283.
- 4 V. Estrella, T. Chen, M. Lloyd, J. Wojtkowiak, H. H. Cornnell, A. Ibrahim-Hashim, K. Bailey, Y. Balagurunathan, J. M. Rothberg, B. F. Sloane, J. Johnson, R. A. Gatenby and R. J. Gillies, *Cancer Res.*, 2013, **73**, 1524–1535.
- 5 W. Duan, Q. Yue, Y. Liu, Y. Zhang, Q. Guo, C. Wang, S. Yin, D. Fan, W. Xu, J. Zhuang, J. Gong, X. Li, R. Huang, L. Chen, S. Aime, Z. Wang, J. Feng, Y. Mao, X.-Y. Zhang and C. Li, *Chem. Sci.*, 2020, **11**, 4397–4402.
- 6 L. Han, W. Duan, X. Li, C. Wang, Z. Jin, Y. Zhai, C. Cao, L. Chen, W. Xu, Y. Liu, Y.-Y. Bi, J. Feng, Y. Mao, Q. Yue, X.-Y. Zhang and C. Li, *ACS Appl. Mater. Interfaces*, 2019, **11**, 15241–15250.
- 7 X. Gao, Q. Yue, Z. Liu, M. Ke, X. Zhou, S. Li, J. Zhang, R. Zhang, L. Chen, Y. Mao and C. Li, *Adv. Mater.*, 2017, **29**, 1603917.
- 8 S. A. Patel and A. J. Minn, *Immunity*, 2018, **48**, 417–433.
- 9 J. Han and K. Burgess, *Chem. Rev.*, 2010, **110**, 2709–2728.
- 10 Z. Guo, S. Park, J. Yoon and I. Shin, *Chem. Soc. Rev.*, 2014, **43**, 16–29.
- 11 J. Zhang, Z. Liu, P. Lian, J. Qian, X. Li, L. Wang, W. Fu, L. Chen, X. Wei and C. Li, *Chem. Sci.*, 2016, **7**, 5995–6005.
- 12 A. Ramesh, S. Kumar, A. Brouillard, D. Nandi and A. Kulkarni, *Adv. Mater.*, 2020, **32**, e2000648.
- 13 A. G. White, B. D. Gray, K. Y. Pak and B. D. Smith, *Bioorg. Med. Chem. Lett.*, 2012, **22**, 2833–2836.
- 14 J. E. Mathejczyk, J. Pauli, C. Dullin, U. Resch-Genger, F. Alves and J. Napp, *J. Biomed. Opt.*, 2012, **17**, 076028.
- 15 Y. Li, Y. Wang, S. Yang, Y. Zhao, L. Yuan, J. Zheng and R. Yang, *Anal. Chem.*, 2015, **87**, 2495–2503.
- 16 V. Wycisk, K. Achazi, P. Hillmann, O. Hirsch, C. Kuehne, J. Darnedde, R. Haag and K. Licha, *ACS Omega*, 2016, **1**, 808–817.
- 17 F. Xue, Y. Wen, P. Wei, Y. Gao, Z. Zhou, S. Xiao and T. Yi, *Chem. Commun.*, 2017, **53**, 6424–6427.
- 18 S. A. Hilderbrand, K. A. Kelly, M. Niedre and R. Weissleder, *Bioconjugate Chem.*, 2008, **19**, 1635–1639.
- 19 K. J. Clear, K. Virga, L. Gray and B. D. Smith, *J. Mater. Chem. C*, 2016, **4**, 2925–2930.
- 20 M. E. Cooper, S. Gregory, E. Adie and S. Kalinka, *J. Fluoresc.*, 2002, **12**, 425–429.
- 21 M. S. Briggs, D. D. Burns, M. E. Cooper and S. J. Gregory, *Chem. Commun.*, 2000, 2323–2324, DOI: 10.1039/b007108k.
- 22 X. Yin, K. Liu, Y. Ren, R. A. Lalancette, Y. L. Loo and F. Jakle, *Chem. Sci.*, 2017, **8**, 5497–5505.
- 23 E. Gaggelli, H. Kozłowski, D. Valensin and G. Valensin, *Chem. Rev.*, 2006, **106**, 1995–2044.



- 24 M. Tafani, J. A. Cohn, N. O. Karpinich, R. J. Rothman, M. A. Russo and J. L. Farber, *J. Biol. Chem.*, 2002, **277**, 49569–49576.
- 25 C. R. Raetz and C. Whitfield, *Annu. Rev. Biochem.*, 2002, **71**, 635–700.
- 26 R. A. Velapoldi and H. H. Tonnesen, *J. Fluoresc.*, 2004, **14**, 465–472.
- 27 D. S. Pisoni, L. Todeschini, A. C. Borges, C. L. Petzhold, F. S. Rodembusch and L. F. Campo, *J. Org. Chem.*, 2014, **79**, 5511–5520.
- 28 C. Bouteiller, G. Clave, A. Bernardin, B. Chipon, M. Massonneau, P. Y. Renard and A. Romieu, *Bioconjugate Chem.*, 2007, **18**, 1303–1317.
- 29 J. Cao, J. Chi, J. Xia, Y. Zhang, S. Han and Y. Sun, *ACS Appl. Mater. Interfaces*, 2019, **11**, 25720–25729.
- 30 S. P. Gromov, M. V. Fomina, A. S. Nikiforov, A. I. Vedernikov, L. G. Kuz'mina and J. A. K. Howard, *Tetrahedron*, 2013, **69**, 5898–5907.

